# Lower crustal crystallization and melt evolution at mid-ocean ridges

V.D. Wanless[1]* & A.M. Shaw[1]

1. Department of Geology and Geophysics, Woods Hole Oceanographic Institution, 360 Woods Hole Road, Woods Hole, MA 02543, USA

**Mid-ocean ridge magma is produced when Earth's mantle rises beneath the ridge axis and melts as a result of the decrease in pressure. This magma subsequently undergoes cooling and crystallization to form the oceanic crust. However, there is no consensus on where within the crust or upper mantle crystallization occurs[1-5]. Here we provide direct geochemical evidence for the depths of crystallization beneath ridge axes of two spreading centres located in the Pacific Ocean: the fast-spreading-rate East Pacific Rise and intermediate-spreading-rate Juan de Fuca Ridge. Specifically, we measure volatile concentrations in olivine-hosted melt inclusions to derive vapour-saturation pressures and to calculate crystallisation depth. We also analyse the melt inclusions for major and trace element concentrations, allowing us to compare the distributions of crystallisation and to track the evolution of the melt during ascent through the oceanic crust. We find that most crystallisation occurs within a seismically-imaged melt lens located in the shallow crust at both ridges, but over 25% of the melt inclusions have crystallisation pressures consistent with formation in the lower oceanic crust. Furthermore, our results suggest that melts formed beneath the ridge axis can be efficiently mixed and undergo olivine crystallisation in the mantle, prior to ascent into the ocean crust.**

Many fast- and intermediate-spreading centers are characterized by a thin (tens of meters), shallow crustal magma chamber beneath the ridge axis[6-8]. This melt lens plays a

key role in controlling the composition of lavas erupted at a ridge axis, as it provides a reservoir in which incremental melts produced during decompression melting[9] can be pooled prior to eruption[10-12]. The crust below the melt lens consists of ~2–18% melt within a network of phenocrysts[13] and is often referred to as the mush zone[12]. One end-member model for lower crustal accretion suggests that all mush zone phenocrysts crystallize in the shallow melt lens and then subside through downward/outward flow to create the lower oceanic crust[1-3]. However, this top-down ("gabbro glacier") model advocating focused accretion has been challenged in favor of distributed accretion models in which crystallization occurs over a range of depths within the crust[4,5,12]. These models suggest that the lower crust forms via *in situ* crystallization through (1) continuous fractional crystallization of melts during ascent through the crust[12] and/or (2) injection of melts in a series of sills that crystallize to various extents throughout the crust [4,5].

To determine where melts crystallize and how melt compositions evolve within the crust, we examined major, trace, and volatile concentrations in 163 olivine-hosted melt inclusions (melt trapped in crystallizing mineral phases) from two magmatically robust mid-ocean ridges (MORs): the fast-spreading northern East Pacific Rise (EPR) and the intermediate-spreading southern Juan de Fuca Ridge (JdFR). Volatile contents ($CO_2$ and $H_2O$) can be used to calculate pressures of melt entrapment in phenocrysts, assuming that the melt is vapor-saturated[14]. Using this approach, we estimate depths of crystallization for melt inclusions from four ridge segments where shallow axial magma chambers have been imaged seismically: EPR 9°50'N (melt lens depth ~1.4 km below seafloor; bsf)[7], EPR 12°48'N (~1.5 km bsf)[6], JdFR Cleft segment (~2.0 km bsf)[8], and

JdFR Vance segment (~2.7 km bsf)[8]. In general, the depth to the melt lens is greater at the JdFR, where slower spreading rates result in cooler crust and thicker axial lithosphere[3]. Geophysical studies at 9°50'N (EPR) also suggest a second, deeper melt lens exists at ~5.4 km bsf, corresponding to the approximate depth of the crust-mantle transition[13].

Volatile concentrations of the melt inclusions indicate that crystallization occurs over a wide range of depths regardless of spreading rate (Fig. 1). Crystallization depths range from 291 to 7410 m bsf at 9°50'N (EPR) and from 368 to 9600 m bsf (JdFR); melt inclusions formed at 12°48'N (EPR) exhibit a more limited range of crystallization depths (934 to 2333 m bsf). At both ridges, the greatest percentage of crystallization is coincident with the location of the seismically inferred melt lens (Fig. 2), with ~72% (EPR) and ~51% (EPR) of the total depth estimates indicating crystallization within 1 km of the melt lens. The "peak" in the distribution of crystallization is deeper on the JdFR (~2.5–4 km bsf) compared to the EPR (~1–2.5 km bsf), consistent with thicker, colder lithosphere. Crystallization depths also record shallower signatures at Cleft compared to Vance segment (Fig. 2), in agreement with a deepening of the melt lens from ~2.0 to ~2.7 km[8].

The majority of the remaining melt inclusions (>25% at both ridges) record crystallization depths below the seismically-inferred melt lens (Fig. 2), indicating that crystallization is not restricted to the shallow crust. The percentage of melt inclusions entrapped at a given depth should not be directly interpreted as the percentage of crystallization occurring at that depth, as it is likely more difficult to erupt olivine phenocrysts formed deeper in the system. Thus, the percentage of crystallization

observed in the lower crust is taken as a minimum of the true crystallization distribution—indicating that significant accretion occurs beneath the melt lens. These observations are inconsistent with purely top-down ("gabbro glacier") models[1-3] for crustal accretion, and instead favor distributed accretion, albeit with significant crystallization in the melt lens. Interestingly, all melt inclusions from 12°48'N have shallow crystallization depths. This may indicate a sampling bias where only olivines crystallizing in the melt lens are incorporated into the erupting magmas or it may suggest that in some instances shallow crystallization is the dominant accretion process. Few melt inclusions have crystallization pressures above the melt lens (< 5%), suggesting that little crystallization occurs during ascent to the seafloor (Fig. 2).

A key assumption in using volatile concentrations to estimate crystallization depths is that the melt inclusions are vapor-saturated. Studies modeling bubble nucleation/growth suggest that melts formed in the upper mantle become super-saturated with $CO_2$ by factors of up to 1.5 at depths of ~20-45 km[15,16]. At these super-saturation ratios, calculations suggest that bubbles nucleate rapidly resulting in degassing of $CO_2$ until vapor-saturation is reached. In these models, rising melts remain saturated until they reach the melt lens; however, super-saturation can occur during the rapid ascent of magmas from the melt lens to the seafloor[15,17-19] (see Methods). This is consistent with vapor-saturation pressures calculated for our host-glasses, which lie between the melt lens and seafloor (Fig. 1). However, no glasses have saturation pressures below the melt lens, suggesting that seafloor eruptions are fed from the melt lens (Fig. S6). In contrast, magmas may have anomalously low vapor-saturation pressures if the initial mantle melt was under-saturated. Olivine-hosted melt inclusions erupted in the Siqueiros transform

fault (EPR) suggest that the MORB source mantle may include an under-saturated component[20]; however, under-saturation is not observed in other studies of volatiles in melt inclusions[21] or basaltic glasses[17-19]. We find no evidence for under-saturation in our data set (all calculated pressures are greater than the corresponding seafloor; Fig. 1), suggesting that melts originating beneath the center of a ridge segment are not under-saturated. Therefore, we infer that the vapor-saturation pressures derived from our melt inclusions provide a reasonable estimate of pressure of inclusion entrapment.

We use crystallization depths, combined with major and trace element data to evaluate magma compositions prior to homogenization in the melt lens and to assess melt evolution during ascent through the crust (Fig. 3). Lavas erupted at fast-spreading ridges generally have less compositional variability than those from slow-spreading ridges; this is commonly attributed to efficient homogenization of melts in shallow magma chambers at fast-spreading ridges[10-12]. Melts entering the base of the crust at all spreading rates, however, may have significant chemical variability, reflecting compositions produced via fractional melting over the entire melting regime[9,22]. Thus, this compositional variability should be preserved in melt inclusions formed below or in the absence of a melt lens. This hypothesis is supported by the wide range of compositions observed in melt inclusions from the Mid-Atlantic Ridge (MAR)[23], which typically lacks a steady-state magma chamber. However, trace element compositions of melt inclusions from a magmatically robust segment of the ultraslow-spreading Gakkel Ridge are remarkably homogeneous, indicating that melts from ultraslow-spreading systems can be homogenized in the mantle prior to crystallization[21].

Melt inclusion compositions from individual locations/eruptions at the EPR and JdFR are relatively limited compared to the MAR[23] (Fig. S4), show no consistent variation with depth in the crust (Fig. 3), and can be explained primarily by fractional crystallization from a single parent melt composition (Figs. S1 and S2). At both EPR locations, melt inclusions have normal mid-ocean ridge basalt (N-MORB) compositions with relatively limited La/Yb ratios (0.90 to 1.91; Fig. 3c) compared to the MAR (La/Yb 0.28–4.0)[23], however, the 2005–2006 melt inclusions are less variable than 1991 melt inclusions (Fig. 3c). Similarly, with the exception of one depleted sample (La/Yb = 0.35), melt inclusions from the JdFR have relatively uniform La/Yb ratios (1.0 to 1.5) that increase slightly with decreasing depth in the crust (Fig. 3). This overall lack of variability in trace element ratios either suggests that initial melts formed in the mantle beneath the ridge axis are relatively homogeneous (batch melting) or that melts with variable compositions are commonly homogenized in the mantle prior to crystallization. There is abundant evidence of fractional melting beneath MORs[9]; therefore, we favor the latter model in which incremental fractional melts are pooled in the mantle before entering the crust. Moreover, melts entering the crust (~5.4 km bsf on the EPR[13]) are more evolved (Mg# $\leq$ 68) than melts in equilibrium with mantle peridotite (Mg# >70[12]), suggesting that significant crystallization occurs in the mantle (Fig. 3b).

The crust-mantle transition likely generates a permeability barrier[4], which facilitates melt pooling, homogenization and crystallization prior to ascent into the overlying crust. This is consistent with geophysical evidence of melt aggregation at the base of the oceanic crust near 9º50'N (EPR) from both compliance[13] and seismic[24] studies. Furthermore, frozen melt bodies are observed in seismic data off-axis at the

crust-mantle transition[25] and there is geologic evidence of melt pooling at the base of the crust in ophiolites[5,26]. Although melt inclusion data from the EPR and JdFR do not show a deep, secondary crystallization peak at the base of the crust (Fig. 2), this may reflect the difficulty in transporting and erupting olivine phenocrysts from below the crust-mantle transition. An alternative mechanism for homogenization is that magma mixing occurs during melt extraction or migration through the mantle, possibly within a decompaction channel that forms at the base of the lithosphere as melts are transported toward the ridge axis[27,28].

This study shows that melts can be efficiently pooled and homogenized in the mantle beneath fast- and intermediate-spreading centers (Fig. 3). It is possible that long-lived magma reservoirs at the crust-mantle transition are only thermally viable in magmatically robust spreading environments. This could explain the more diverse range of melt inclusion compositions observed along the MAR[23] compared to the EPR and JdFR. This can also be reconciled with homogeneous Gakkel Ridge melt inclusions[21], as these were erupted along a magmatically robust section of the ultraslow-spreading center. Thus, we hypothesize that melts can be pooled in the mantle beneath magmatically robust sections of ridges at all spreading rates, but is more common at faster-spreading ridges. The longevity of the deep melt lens is likely dependent on magma supply. Therefore, compositional variability of melts entering the crust may fluctuate temporally, accounting for the range of La/Yb ratios in the 1991 eruption (Fig. 3).

Pooled melts may continue to evolve during their ascent through the ocean crust or in the shallow melt lens. However, melt inclusion compositions do not show a simple trend of increasing fractional crystallization with decreasing depth (Fig. 3), which would

result in a general decrease in MgO, CaO, $Al_2O_3$ and Sr depending on the phases saturated in the melt (olivine, plagioclase, and clinopyroxene). This implies that melts are not simply migrating through the ocean crust, while undergoing increasing degrees of fractional crystallization. Our data also show that the more mafic melts measured in the melt inclusions (MgO >9.5) are observed at all depths within the crust, while the more evolved melts are restricted to the shallower crust, in or near the melt lens. Therefore, we favor an accretion model in which some melts ascend through the mush zone without extensive differentiation, while other melts crystallize during ascent (Fig. 4). Additionally, the extent of magma differentiation within the crust may vary with spreading rate, as JdFR melt inclusions are less variable than EPR melt inclusions (Fig. 3).

The combination of melt inclusion compositions and vapor-saturation pressures provides a powerful tool for understanding crustal accretion processes and melt differentiation at MORs. Using this method, we directly determine where within the crust crystallization occurs and track the evolution of melts as they ascend from the mantle through the crust. The “peak” in the crystallization distributions correlates remarkably well with the depth of the melt lens across the different spreading rates. Our melt inclusion data indicate that there are two regions of melt pooling beneath the ridge axis and clearly show that homogenization is not restricted to shallow magma chambers. This calls into question fundamental assumptions regarding the magmatic plumbing systems beneath fast-spreading MORs and the processes that lead to the relatively limited lava compositions. Additionally, this technique may be used to determine if there are regions of melt homogenization at slower spreading ridges, where seismic imaging of a magma lens is difficult.

*Methods:* A total of 163 naturally glassy, olivine-hosted, melt inclusions, host-olivines and 12 associated glasses from the EPR and JdFR were analyzed for major element and volatile contents (Tables S1, S2, and S4). A total of 62 samples were measured for trace element concentrations (Table S3). Volatile concentrations ($H_2O$, $CO_2$, F, S, Cl) were measured on each glassy melt inclusions using the 1280 ion microprobe at WHOI. Analyses were run using a $Cs^+$ beam and following techniques described in Shaw et al.,[29]. Calibration curves were made for each measurement session and a MORB glass standard (ALV-519-4-1) with compositions similar to the EPR and JdFR melt inclusions, was run routinely throughout the analyses to monitor instrumental drift. Major element concentrations were measured on the JOEL electron microprobe at MIT, using a 10 nA beam intensity, a 10 μm spot size, and a 15kV accelerating voltage. Compositions of host-olivines were also determined using an average of 3 analyses per phenocryst, which included measurements from the melt inclusion to the grain boundary to look for evidence of compositional zoning. Trace element contents were determined on a subset of samples using the 6f ion microprobe at Arizona State University, following methods outlined in Shaw et al.,[21]. Analyses were conducted using a 10 nA focused beam of $O^-$ and energy filtering (-75 eV offset) was applied.

In general, we find relatively low and uniform $H_2O$ concentrations at the EPR (0.10–0.23 wt%) and JdFR (0.12–0.22 wt%), consistent with previous studies of glasses[17,18] and melt inclusions[20] from fast- to intermediate-spreading ridges (Fig. 1). By contrast, $CO_2$ concentrations show considerable variability with values ranging from 127 to 1770 ppm (Fig. 1). Based on volatile contents in each melt inclusion, vapor-saturation

pressures were calculated[14] and converted to crystallization depths taking into account the overlying water pressure and assuming a crustal density of 2.9 g/cm$^3$. The combined accuracy and precision of the volatile measurements result in a 2-sigma error of ~10%, which translates into approximately ±1 km in calculated crystallization depths.

*Vapor-Saturation*: A key to establishing whether vapor-saturation pressures recorded by our melt inclusions reflect the conditions of in situ crystallization is that melts migrating through the upper mantle and lower crust are not super-saturated in $CO_2$. Numerical models suggest that melts below MORs can be super-saturated with $CO_2$ by a factor of 1.5 at depths of ~45 km[15]. However, once this degree of super-saturation is reached, bubble nucleation will initiate, resulting in rapid bubble growth and degassing of $CO_2$ until saturation is reached in the melt[16]. These calculations suggest that super-saturated melts will equilibrate within one half hour, and afterwards melts will remain at saturation as they migrate through the mantle until they reach a crustal magma reservoir. Thus, melt inclusions formed during this ascent should record the saturation pressures corresponding to where the inclusion was trapped.

Once melts reach a shallow magma reservoir, however, greater degrees of super-saturation may be required to initiate bubble growth[16]. Indeed, MOR glasses erupted on the seafloor are often super-saturated, which is attributed to rapid ascent of magmas from the crustal melt lens to the seafloor via dikes[17-19]. Such rapid ascent rates are not typically considered appropriate for melt ascent below the melt lens[15], however, rapid ascent (and thus super-saturation) cannot be ruled out. Therefore, to test the possibility that melts entering the melt lens are super-saturated, we examined the maximum

saturation pressures of erupted lavas at a number of ridge segments (including those in our study) where the melt lens has been determined seismically.

If super-saturated melts are entering shallow magma chambers, we would expect that some of the glasses erupted from the chamber would preserve these conditions. Compiling all MOR glasses from the EPR and JdFR with $CO_2$ and $H_2O$ data and known melt lens depths from PetDB, we find that none have saturation pressures below the seismically imaged melt lens (Fig. S6). However, 25% of our melt inclusions indicate either deeper crystallization or entrapment of super-saturated melts. It would seem rather fortuitous that no basalts preserve these conditions but ~25% of the melt inclusions formed in the same magma chambers preserve these signatures. Additionally, if the relatively high $CO_2$ melt inclusions entrap super-saturated melts that ascended directly from the mantle or lower crust to the melt lens, then we would expect that these melts would also be less fractionated then melts that have equilibrated within the melt lens. However, we observe no correlation between $CO_2$ (or depth) and Mg# (Fig. S3). Therefore, we conclude that melt inclusions with elevated saturation pressures are the result of entrapment of saturated melts at various depths within the crust and not from entrapment of super-saturated melts within the melt lens.

References

1. Nicolas, A. & Reuber, I. A new magma chamber model based on structural studies in the Oman ophiolite. *Tectonophysics* **151**, 87–105 (1988).

2. Quick, J. & Denlinger, R. Ductile deformation and the origin of layered gabbro in

ophiolites. *Journal of Geophysical Research* **98**, 14015–14027 (1993).

3. Phipps Morgan, J. & Chen, Y. The genesis of oceanic crust: Magma injection, hydrothermal circulation, and crustal flow. *Journal of Geophysical Research* **98**, 6283–6297 (1993).

4. Kelemen, P., Koga, K. & Shimizu, N. Geochemistry of gabbro sills in the crust-mantle transition zone of the Oman ophiolite: implications for the origin of the oceanic lower crust. *Earth and Planetary Science Letters* **146**, 475–488 (1997).

5. Kelemen, P. & Aharonov, E. Periodic formation of magma fractures and generation of layered gabbros in the lower crust beneath oceanic spreading ridges. *Faulting and magmatism at mid-ocean ridges* **106**, 267–289 (1998).

6. Detrick, R. S. *et al.* Multi-channel seismic imaging of a crustal magma chamber along the East Pacific Rise. *Nature* **326**, 35–41 (1987).

7. Kent, G., Harding, A. & Orcutt, J. Distribution of magma beneath the East Pacific Rise between the Clipperton transform and the 9 17′ N Deval from forward modeling of common depth point data. *Journal of Geophysical Research* **98**, 13945–13969 (1993).

8. Canales, J. P. *et al.* Upper crustal structure and axial topography at intermediate spreading ridges: Seismic constraints from the southern Juan de Fuca Ridge. *Journal of Geophysical Research* **110**, 1–27 (2005).

9. Johnson, K. T. M., Dick, H. J. B. & Shimizu, N. Melting in the Oceanic Upper Mantle: An Ion Microprobe Study of Diopsides in Abyssal Peridotites. *Journal of Geophysical Research* **95**, 2661–2678 (1990).

10. O'Hara, M. & Mathews, R. Geochemical Evolution in an Advancing, Periodically

Replenished, Periodically Tapped, Continuously Fractionated Magma Chamber. *Journal of the Geological Society of London* **138**, 237–277 (1981).

11. Batiza, R. *et al.* Steady and non-steady state magma chambers below the East Pacific Rise. *Geophysical Research Letters* **23**, 221–224 (1996).

12. Sinton, J. & Detrick, R. Mid-ocean ridge magma chambers. *Journal of Geophysical Research* **97**, 197–216 (1992).

13. Crawford, W., Webb, S. & Hildebrand, J. Constraints on melt in the lower crust and Moho at the East Pacific Rise, 9 deg 48 min N, using seafloor compliance measurements. *Journal of Geophysical Research* **104**, 2923–2939 (1999).

14. Dixon, J. E. & Stolper, E. M. An Experimental Study of Water and Carbon Dioxide Solubilities in Mid-Ocean Ridge Basaltic Liquids. Part II: Applications to Degassing. *Journal of Petrology* **36**, 1633–1646 (1995).

15. Bottinga, Y. & Javoy, M. Mid-Ocean Ridge Basalt Degassing: Bubble Nucleation. *Journal of Geophysical Research* **95**, 5125–5131 (1990).

16. Bottinga, Y. & Javoy, M. MORB degassing: evolution of CO2. *Earth and Planetary Science Letters* **95**, 215–225 (1989).

17. Dixon, J., Stolper, E. & Delaney, J. R. Infrared spectroscopic measurements of CO2 and H2O in Juan de Fuca Ridge basaltic glasses. *Earth and Planetary Science Letters* **90**, 87–104 (1988).

18. Le Roux, P., Shirey, S., Hauri, E., Perfit, M. & Bender, J. The effects of variable sources, processes and contaminants on the composition of northern EPR MORB (8-10° N and 12-14° N): Evidence from volatiles (H2O, CO2, S) and halogens (F, Cl). *Earth and Planetary Science Letters* **251**, 209–231 (2006).

19. Soule, S. A. *et al.* CO2 variability in mid-ocean ridge basalts from syn-emplacement degassing: Constraints on eruption dynamics. *Earth and Planetary Science Letters* **327-328**, 39–49 (2012).

20. Saal, A., Hauri, E., Langmuir, C. & Perfit, M. Vapour undersaturation in primitive mid-ocean-ridge basalt and the volatile content of Earth's upper mantle. *Nature* **419**, 451–455 (2002).

21. Shaw, A., Behn, M., Humphris, S., Sohn, R. & Gregg, P. Deep pooling of low degree melts and volatile fluxes at the 85° E segment of the Gakkel Ridge: Evidence from olivine-hosted melt inclusions and glasses. *Earth and Planetary Science Letters* **289**, 311–322 (2010).

22. Rubin, K. & Sinton, J. Inferences on mid-ocean ridge thermal and magmatic structure from MORB compositions. *Earth and Planetary Science Letters* **260**, 257–276 (2007).

23. Shimizu, N. The geochemistry of olivine-hosted melt inclusions in a FAMOUS basalt ALV519-4-1. *Physics of the Earth and Planetary Interiors* **107**, 183–201 (1998).

24. Dunn, R., Toomey, D. & Solomon, S. C. Three-dimensional seismic structure and physical properties of the crust and shallow mantle beneath the East Pacific Rise at 9 30'N. *Journal of Geophysical Research* **105**, 23,537–23,555 (2000).

25. Nedimović, M. R. *et al.* Frozen magma lenses below the oceanic crust. *Nature* **436**, 1149–1152 (2005).

26. Karson, J., Collins, J. & Casey, J. Geologic and Seismic Velocity Structure of the Crust Mantle Transition in the Bay of Islands Ophiolite Complex. *Journal of*

*Geophysical Research* **89**, 6126–6138 (1984).

27. Klein, E. Geochemistry of the Igneous Oceanic Crust. *The crust: treatise on geochemistry* **3**, 433–464 (2005).

28. Sparks, D. W. & Parmentier, E. M. Melt extraction from the mantle beneath spreading centers. *Earth and Planetary Science Letters* **105**, 368–377 (1991).

29. Shaw, A. M., Hauri, E. H., Fischer, T. P., Hilton, D. R. & Kelley, K. A. Hydrogen isotopes in Mariana arc melt inclusions: Implications for subduction dehydration and the deep-Earth water cycle. *Earth and Planetary Science Letters* **275**, 138–145 (2008).

30. Newman, S. & Lowenstern, J. VC: a silicate melt-H2O-CO2 solution model written in Visual Basic for excel*. *Computers & Geosciences* **28**, 597–604 (2002).

**Corresponding author:** V. D. Wanless (dwanless@whoi.edu)

**Acknowledgements**: We thank R. Hervig, B. Montelone, N. Shimizu, and N. Chatterjee for their assistance with geochemical analyses. M. Behn and A. Soule are thanked for their comments and discussions. This research was supported by the National Science Foundation (EAR-0646694) and the WHOI Deep Ocean Exploration Institute/Ocean Ridge Initiative.

**Author contributions**: V.D.W. prepared samples. V.D.W and A.M.S. collected geochemical data. V.D.W. and A.M.S. worked together on data interpretations and preparation of the manuscript.

Figure Captions

**Figure 1 $CO_2$ (ppm) versus $H_2O$ (wt%) for melt inclusions and associated glasses from the (a) EPR and (b) JdFR:** Vapor-saturation curves (black lines) for a range of pressures (200–2500 bars) calculated from Newman and Lowenstern[30]. No melt inclusions or glasses have pressures greater than the seafloor (~250 bars; dashed black line), suggesting that the melts are not under-saturated. Vapor-saturation calculations indicate a wide range of crystallization pressures from the seafloor to >2500 bars. In contrast, erupted glasses have lower pressures, ranging from the top of the melt lens to the seafloor.

**Figure 2 Histograms showing the distribution of crystallization depths of melt inclusions from the (a) EPR and (b) JdFR:** Depths were estimated using vapor-saturation pressures, accounting for the overlying water column and a crustal density of 2.9 g/cm$^3$. A statistically determined bin size of 1500 m is used (see supplementary material); however, changing the bin size (1000–2000 m) does not significantly change the overall shape of the histograms (Figure S3). The melt lens depth is shown for each ridge[7,8]. Over 50% of the melt inclusions have crystallization depths consistent with formation in/near the melt lens (± 1 km), however, >25% crystallized in the lower crust or upper mantle.

388 **Figure 3 Major Elements Versus Depth:** Melt inclusion and glass compositions for the
389 (a, b, c) EPR and (d, e, f) JdFR versus crystallization depth below seafloor (bsf).
390 Symbols are the same as Figure 1 and errors on depth measurements are provided. Melt
391 lens depths are shown as dashed lines. We find no trend of increasing fractional
392 crystallization with decreasing depth in the crust; however, compositions are more
393 variable in the shallow crust. (a, d) $Al_2O_3$ concentrations show no evidence of plagioclase
394 crystallization or assimilation. $La_N/Yb_N$ ratios (c, f) are relatively limited for each
395 location/eruption, suggesting that melts are pooled and homogenized in the mantle.
396 Average N-MORB[27] (0.49) and E-MORB[27] (3.1) are shown.
397
398 **Figure 4 Schematic diagram of crustal accretion at fast-spreading centers based on**
399 **melt inclusions analyses:** The shallow melt lens (orange) forms at the base of the
400 sheeted dikes (grey) but would be deeper at JdFR compared to EPR. A deeper region of
401 melt pooling (red) beneath the ridge homogenizes fractional mantle melts prior to
402 crystallization in the crust. Melts may crystallize to variable degrees during ascent
403 (dashed arrows) or may ascend with little to no differentiation (solid arrow). Sills may
404 form within in the lower crust; however, the formation of sills is not required to explain
405 the melt inclusions data.
406

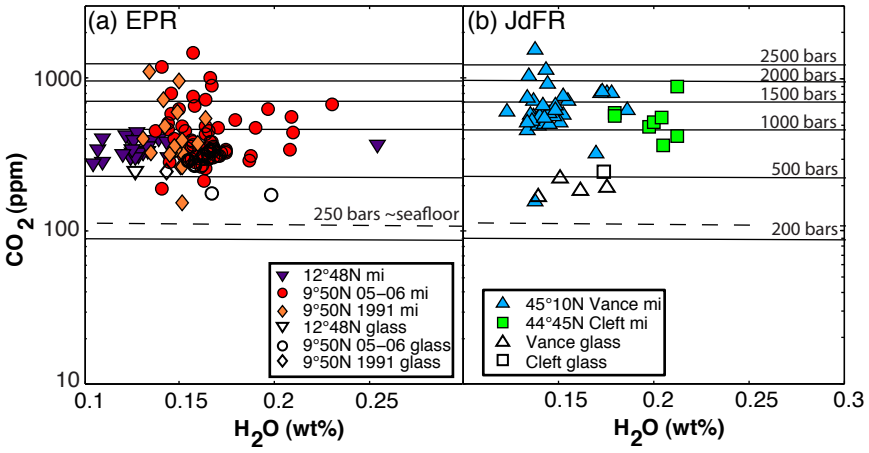
(a) EPR
(b) JdFR
1000
100
10
$CO_2$ (ppm)
2500 bars
2000 bars
1500 bars
1000 bars
500 bars
200 bars
250 bars ~seafloor
12°48N mi
9°50N 05–06 mi
9°50N 1991 mi
12°48N glass
9°50N 05–06 glass
9°50N 1991 glass
45°10N Vance mi
44°45N Cleft mi
Vance glass
Cleft glass
0.1
0.15
0.2
0.25
0.15
0.2
0.25
0.3
$H_2O$ (wt%)
$H_2O$ (wt%)

Figure 1

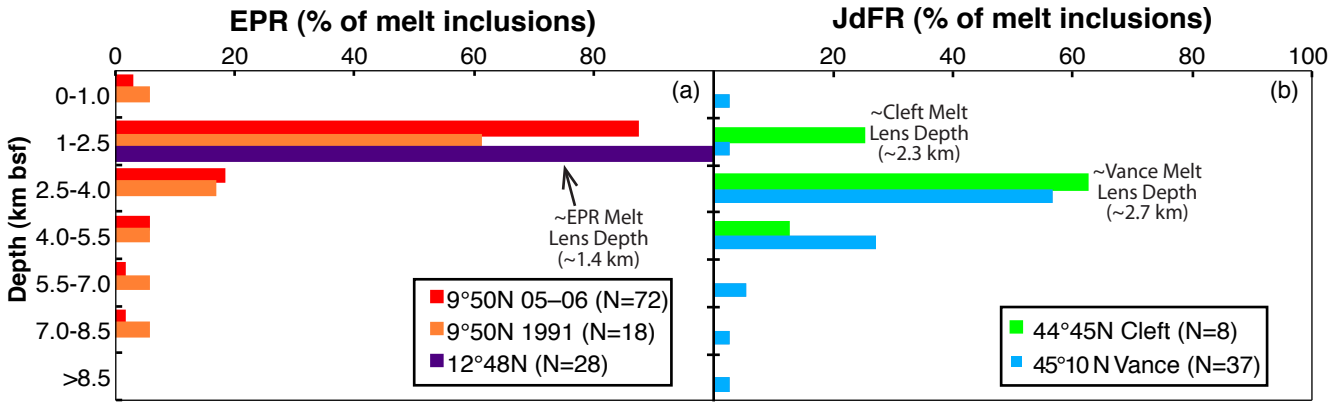
EPR (% of melt inclusions)
JdFR (% of melt inclusions)
Depth (km bsf)
0-1.0
1-2.5
2.5-4.0
4.0-5.5
5.5-7.0
7.0-8.5
>8.5
0
20
40
60
80
100
(a)
(b)
~EPR Melt Lens Depth (~1.4 km)
~Cleft Melt Lens Depth (~2.3 km)
~Vance Melt Lens Depth (~2.7 km)
9°50N 05–06 (N=72)
9°50N 1991 (N=18)
12°48N (N=28)
44°45N Cleft (N=8)
45°10 N Vance (N=37)

Figure 2

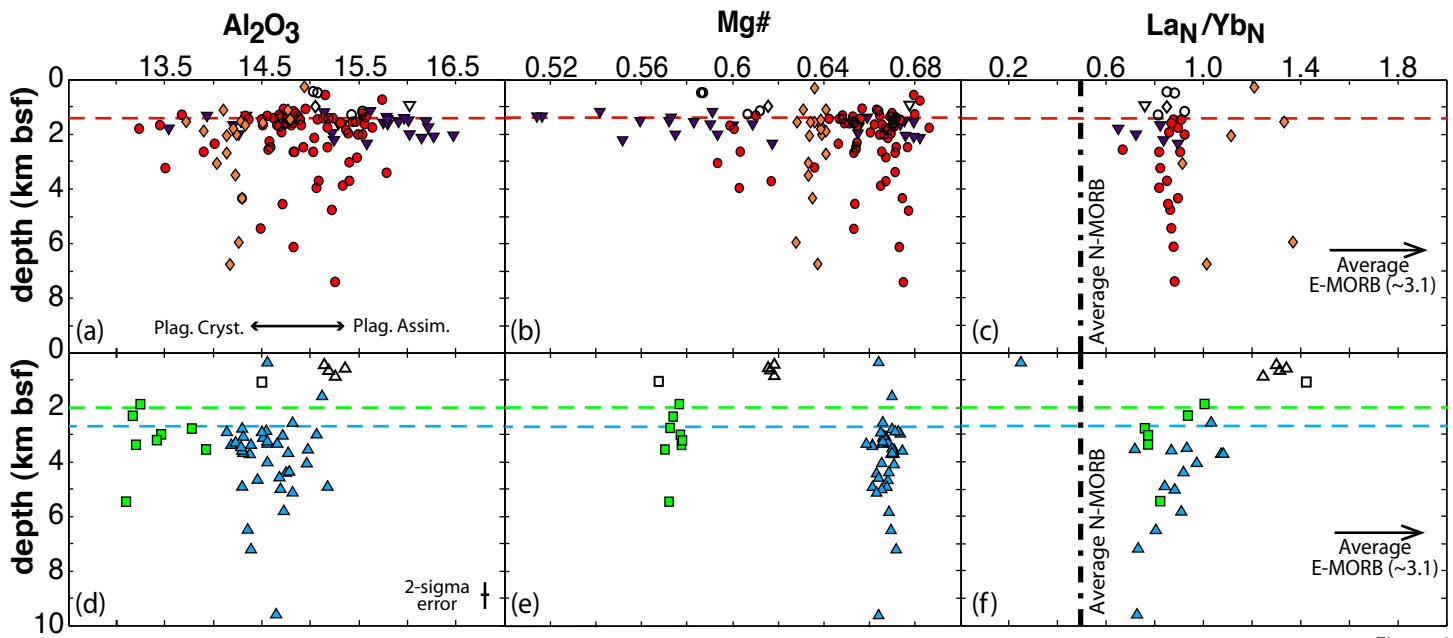
Al2O3
13.5
14.5
15.5
16.5
Mg#
0.52
0.56
0.6
0.64
0.68
LaN/YbN
0.2
0.6
1.0
1.4
1.8
depth (km bsf)
0
2
4
6
8
10
(a)
Plag. Cryst.
Plag. Assim.
(b)
(c)
Average N-MORB
Average
E-MORB (~3.1)
(d)
2-sigma
error
(e)
(f)

Figure 3

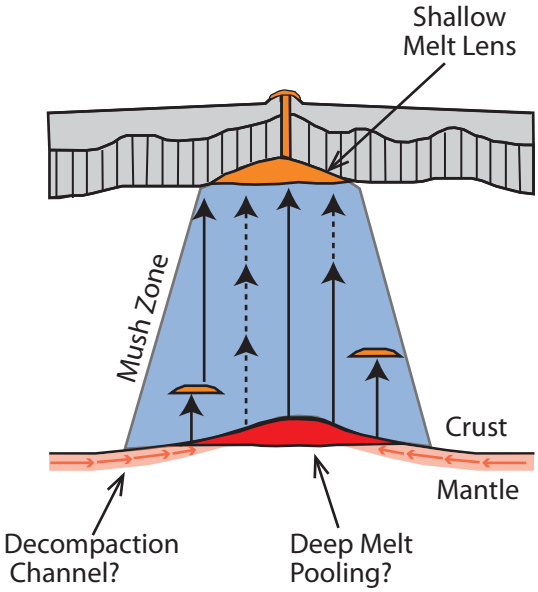
Shallow
Melt Lens
Mush Zone
Crust
Mantle
Decompaction
Channel?
Deep Melt
Pooling?

Figure 4